



Ice Breakup Controls Dissipation of Wind Waves Across Southern Ocean Sea Ice

Fabrice Ardhuin, Mark Otero, Sophia Merrifield, Antoine Grouazel, Eric Terrill

► To cite this version:

Fabrice Ardhuin, Mark Otero, Sophia Merrifield, Antoine Grouazel, Eric Terrill. Ice Breakup Controls Dissipation of Wind Waves Across Southern Ocean Sea Ice. *Geophysical Research Letters*, 2020, 47 (13), 10.1029/2020GL087699 . hal-03094089

HAL Id: hal-03094089

<https://hal.science/hal-03094089>

Submitted on 4 Jan 2021

HAL is a multi-disciplinary open access archive for the deposit and dissemination of scientific research documents, whether they are published or not. The documents may come from teaching and research institutions in France or abroad, or from public or private research centers.

L'archive ouverte pluridisciplinaire **HAL**, est destinée au dépôt et à la diffusion de documents scientifiques de niveau recherche, publiés ou non, émanant des établissements d'enseignement et de recherche français ou étrangers, des laboratoires publics ou privés.

Fabrice Ardhuin¹, Mark Otero¹, Sophia Merrifield¹, Antoine Grouazel², and
Eric Terrill¹

²Univ. Brest, CNRS, IRD, Ifremer, Laboratoire d'Océanographie Physique et Spatiale (LOPS), IUEM, Brest, France

8
9
10
11
12
13

- Wind-waves attenuate across the Antarctic sea ice with a narrow directional distribution
- Scattering of waves by ice floes plays a negligible role in wave attenuation
- Observed wave attenuation is consistent with ice break-up modulating the dissipation strength

–1–

Abstract

Sea ice inhibits the development of wind-generated surface gravity waves which are the dominant factor in upper ocean mixing and air-sea fluxes. In turn, sea ice properties are modified by wave action. Understanding the interaction of ice and waves is important for characterizing both air-sea interactions and sea ice dynamics. Current leading theory attributes wave attenuation primarily to scattering by ice floes. Here we use new *in situ* wave measurements to show that attenuation is dominated by dissipation with negligible effect by scattering. Time series of wave height in ice exhibit an “on/off” behavior that is consistent with switching between two states of sea ice; a relatively unbroken state associated with strong damping (off), possibly caused by ice flexure, and very weak attenuation (on) across sea ice that has been broken up by wave action.

Plain Language Summary

Waves created by wind at the ocean surface are strongly attenuated when they travel across ice-covered regions. Until now, this effect was thought to be the result of waves reflection off pieces of ice. Using new measurements of wave directions, we show that waves do not come from a broad range of directions, and scattering must be weak. Instead we find that attenuation is highly variable and related to the size of ice floes. We hypothesize that attenuation may be caused by cyclic deformation of the ice. When the waves are large enough to break the ice up, this deformation stops and the attenuation is much less. This finding is important for forecasting waves in ice-infested waters as well as predicting seasonal sea ice extent.

1 Introduction

Recent studies have revealed that ocean waves play a significant role in the ice momentum balance [Stopa *et al.*, 2018], ice extent [Kohout *et al.*, 2014], and the rapid thickening of ice when the ocean freezes [Sutherland and Dumont, 2018]. Previous wave measurements in ice-covered waters [Doble and Bidlot, 2013; Kohout *et al.*, 2014] have shown that waves in ice attenuate over longer distances when the open water wave height increases, often due to longer corresponding wave periods [Meylan *et al.*, 2014]. This result was used to define an *ad hoc* parameterization of wave attenuation [Kohout *et al.*, 2016] that fails to reproduce the large range of observed attenuations for any given off-ice wave height and wave period [Stopa *et al.*, 2018]. This poor performance calls for a detailed physical understanding of ice-wave interaction processes.

Following early works [Wadhams, 1988], the attenuation of waves that propagate under the ice is generally attributed to scattering [Squire, 2020]. Scattering is a partial reflection of waves at the boundaries of ice floes, broadening the distribution of wave directions. Other processes dissipate wave energy into heat and narrow the wave direction distribution around the shortest propagation path. Measured wave directions within the ice can thus reveal the importance of scattering. For example, the narrow directional spread of waves with periods 19 to 23 s measured with directional tilt-meters in the Arctic showed that scattering could not be a significant source of attenuation for these very long waves [Ardhuin *et al.*, 2016]. Here we generalize these observations to more typical wave periods from 10 to 20 s using wave buoy measurements. We evaluate two different dissipation processes: under-ice friction [Stopa *et al.*, 2016], and the anelastic dissipation associated with ice flexure [Cole *et al.*, 1998]. The latter process yields large dissipation rates when the ice is flexing. However, flexing only occurs for waves shorter than about twice the ice floe diameter as floes tilt over longer waves [Boutin *et al.*, 2018]. This varying behavior as a function of wavelength can explain the observed sudden drop in wave attenuation when ice is broken by waves [Collins *et al.*, 2015]. Here the floe sizes are constrained by Synthetic Aperture Radar (SAR) imagery.

2 Measured wave properties and sea ice conditions

Freely drifting wave buoys [Drazen *et al.*, 2016] were deployed in the Southern Ocean in 2018, and advected into advancing sea ice. Fig. 1.a shows the positions of three buoys numbered 623, 624 and 625. Successive positions of the ice edge, defined as the 15% ice concentration contour, are estimates from the Advanced Microwave Scanning Radiometer 2 (AMSR2) radiometer [Spreen *et al.*, 2008].

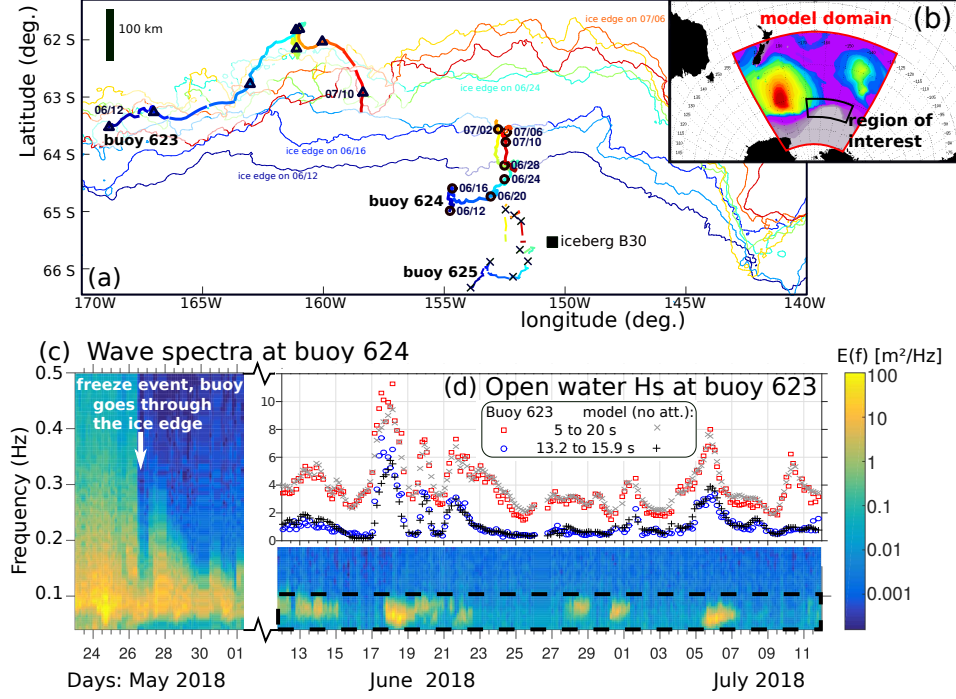


Figure 1. (a) Positions of the ice edge, defined as the 15% ice concentration contour, every 4 days from June 12 to July 10, 2018, and positions of three mini-buoys, number 623 (triangles in open water), 624 (circles in the ice) 625 (crosses, further in the ice). (b) Geographical context and domain of the numerical wave model used in section 3. The black rectangle corresponds to the region shown in (a), the colors show simulated significant wave heights from 0 to 10 m on July 4th at 12:00 UTC. (c) Wave energy spectra at buoy 624. (d) Time series of measured and modeled wave height at the open water buoy 623 for period ranges 5 to 20 s, and 13.2 to 15.9 s. See also supplementary video S1.

Buoy 624 measured a typical wave signal as shown in Fig. 1.c. High wave frequencies (above 0.3 Hz) vanish once the buoy is a few kilometers into the ice on May 26. This attenuation is similar to other measurements obtained during the formation of meter-scale rafts of ice known as pancakes [Thomson *et al.*, 2018]. Frequencies between 0.10 and 0.30 Hz gradually disappear as the buoy gets deeper into the ice, 80 km from the ice edge on June 12. This evolution is presumably associated with the progressive welding of pancakes into much larger floes forming solid plates that can extend over kilometers. After June 12, only frequencies under 0.1 Hz are episodically recorded as the ice margin continues to extend further offshore reaching a distance of 150 km from 624 by June 24. Wave energy exceeds the instrument noise floor during seven events observed by 624; each of which is associated with a storm (Fig. 2.a). Buoy 625 kept a nearly constant distance south of 624, 120 km further into the ice field,

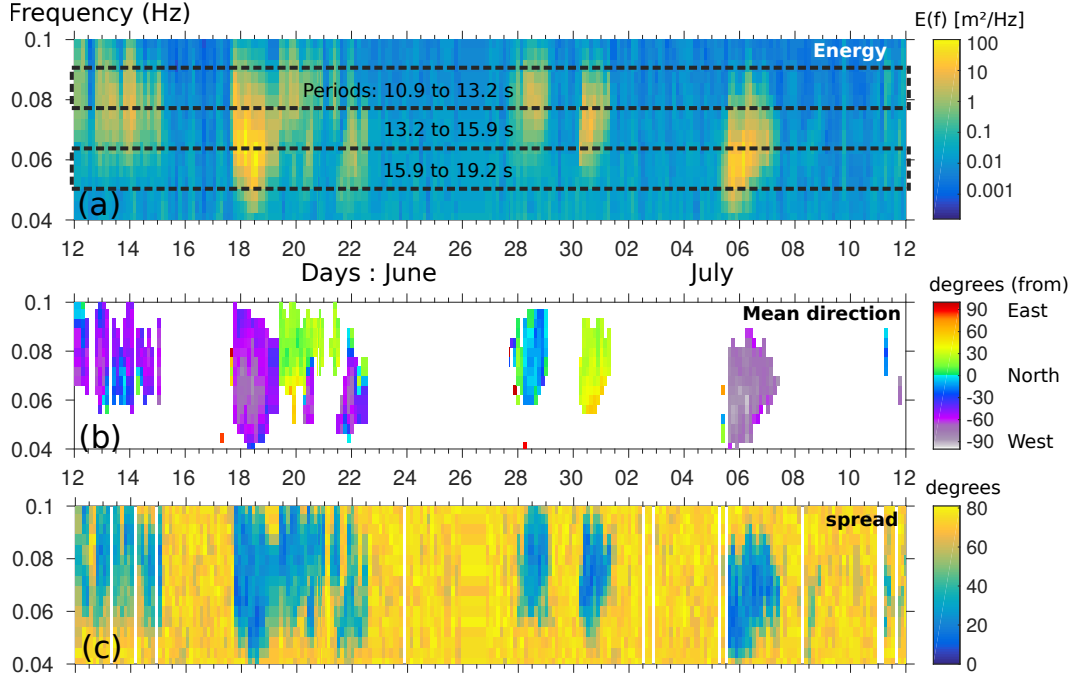


Figure 2. Wave properties measured by buoy 624 as a function of time and frequency. (a) Energy spectrum, with dotted boxes around the short and long period ranges used in Fig. 4, (b) Mean directions, shown when the energy is above -10 dB, avoiding random noise for low energies. (c) directional spread.

until its trajectory crosses iceberg B30 on July 14. This 30 km long iceberg is clearly visible in all the AMSR2 images as it cuts a wake of open water in the sea ice. Before July 13, buoy 623 was out of the ice, providing measurements representative of open water. A numerical model simulation without ice attenuation shows good agreement with these measurements (Fig. 1.d). This model is used to quantify the time delay and dispersion due to propagation from open water (buoy 623) into the ice (buoys 624 and 625). The difference between the model and observations can then be attributed to wave-ice interaction processes.

The wave height observed within the ice is not a simple function of the open water measurements, as shown in Fig. 1.d. The attenuation from open water to buoy 624 depends on the wave frequency and direction. Attenuation is stronger for higher frequencies. Attenuation is also stronger when waves travel a longer distance under the ice, namely when their directions are more oblique relative to the ice edge (e.g. from the West, in grey-purple colors on July 4–7, Fig. 2.b). The buoy measures narrow directional distributions with spreads under 20 degrees (blues in Fig. 2.c) as soon as the energy level exceeds $0.1 \text{ m}^2/\text{Hz}$. The measured waves are thus similar to open ocean swell with long crests and a narrow range of propagation directions.

We now turn to Sentinel-1 radar imagery for information on ice properties. These SAR images were analyzed for two types of features (Fig. 3).

First we determined the presence (blue symbols) or absence (red symbols) of leads. Leads are straight features at the boundaries of large scale floes that may correspond to an ice-free surface, which appear as dark bands, or that can re-freeze and appear bright due to the presence of frost flowers. When leads are visible, the diameters of floes exceed 1 km and waves have not been able to break the ice. In the absence of

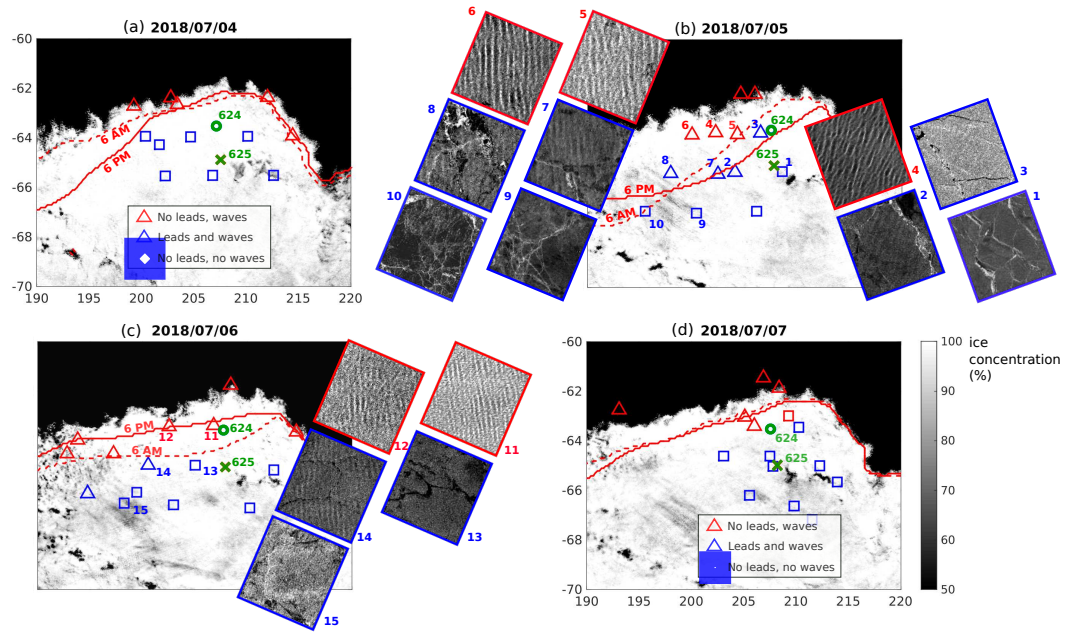


Figure 3. Daily maps of ice concentrations from AMSR2 - ASI, as provided by University of Bremen), here position and locations of Sentinel 1 Wave Mode SAR imagery classified by the presence of leads and waves, through a storm event from (a) July 4th to (d) July 7th. Each SAR image is represented by a blue symbol if leads are detected, red if no lead is detected, triangles if waves are visible, squares otherwise. For some of the images, numbered 1 to 15, sub-sets of the SAR images are also shown. Each subset is 5 km by 5 km and full images are shown in Fig. S1-S15. Finally, the contour of maximum floe diameter $D_{max} = 300$ m, as estimated from the model run using aerodynamic dissipation, is shown with a dashed line at 6 AM and solid line at 6 PM marking the extent of the region where ice is broken by waves in the model.

leads, it is expected that ice is broken into small floes and their differential advection yields a horizontally uniform brightness. The second type of feature is wave patterns. Images numbered 4–6 acquired on July 5 clearly show a wave field propagating from the West, with a dominant wavelength around 400 m that is reduced to 270 m in images 11, 12 and 14 acquired on July 6. Estimated wave heights [Ardhuin *et al.*, 2017] range from 0.7 to 2.5 m. Much fainter wave patterns are also visible in images 2, 3 and 7. All these wave features are long-crested except in image 8 where ring waves are observed in probable association with reflections off an iceberg. The radar imagery acquired around the trajectories of the buoys thus confirms the penetration, 200 km inside the ice, of long-crested waves with heights on the order of 1 m. Also, we interpret the disappearance of leads towards the ice edge on July 5 and 6 as the result of ice break up by wave action.

3 Interpretation using a wave attenuation and ice break-up mode

The magnitude and a plausible cause of wave attenuation will now be examined with a numerical wave model, based on version 6.05 of the WAVEWATCH III modelling framework [The WAVEWATCH III[®] Development Group, 2019, hereinafter WW3], that is constrained by these ice observations. We consider three model simulations that differ only in their parameterizations of wave-ice interactions:

- A simple "no attenuation" simulation in which the effect of the ice is limited to shutting off the generation of waves by wind forcing and dissipation associated with wave breaking. The difference between the measurements and the "no attenuation" run provides an estimate of the ice-induced attenuation.
- A scattering + viscous basal friction ("S1V1" for short) in which the scattering coefficient is determined by the ice thickness and maximum floe size following Williams *et al.* [2013] with the addition of back-scattering (so that the scattering term conserves energy) and viscous dissipation taken from Liu and Mollo-Christensen [1988] with the viscosity taken to be the molecular viscosity of sea water at the freezing point. Our scattering term conserves wave energy which is isotropically redistributed as discussed in Boutin *et al.* [2018]. Scattering strength is based on the normal reflection of waves travelling from the open ocean under a semi-infinite ice floe with a straight boundary [Williams *et al.*, 2013].
- An anelastic dissipation based on known microscopic rheological properties of dislocations in ice crystals [Cole *et al.*, 1998; Cole, 2020], adapted by Boutin *et al.* [2018] to represent the dissipation of waves when floes with diameters larger than half the wavelength are flexing. This parameterization is combined with viscous basal friction and scattering, with the scattering coefficient reduced by a factor 5.

Apart from the differences in parameterizations, the common features of the three model simulations reported here are a spatial resolution of 0.1 degree in latitude and 0.2 degree in longitude forced at the boundaries (red line in Fig. 1.b) by a 0.5 degree global model. Wind forcing is provided by the European Center for Medium Range Weather Forecasts (ECMWF) operational analyses and forecasts. Ice concentration was provided by AMSR2 with a correction designed to limit the errors caused by atmospheric water vapor [Gloersen and Cavalieri, 1986]: all concentrations above 70% was set to 100%. Based on climatology data, the ice thickness was set to a constant 0.77 m. Given our focus on wave periods longer than 10 s, we neglected the effect of ice on wave dispersion [Collins *et al.*, 2018]. This is discussed in the Supplementary Information. The model uses 24 directions and an exponential frequency grid from 0.037 to 1 Hz.

The ice flexural strength σ_c was adjusted to obtain a position of the break-up front consistent with SAR imagery, as shown in Fig. 3, giving $\sigma_c = 0.6$ MPa.

In all cases the maximum floe size diameter is estimated based on the expected local maximum flexural strength over the model time step of 600 s [Boutin *et al.*, 2018]. This floe size only has an impact on wave dissipation rate in the case of the anelastic simulation.

We also note that other wave-ice interaction effects have been investigated in other studies [Squire, 2020], including ice floe collisions [Herman *et al.*, 2019] or the breaking of steep waves over ice floes [Toffoli *et al.*, 2015]. Although these processes are reasonably important right at the ice edge, we expect them to play only a minor role overall because they are typically non-linear with higher relative dissipation for higher waves, hence leading to a shorter attenuation distance for steeper ocean waves. This is not consistent with available large scale observations that show a constant or weaker attenuation for steeper waves [Meylan *et al.*, 2014; Stopa *et al.*, 2018], and we thus have not considered these processes here.

Modeled wave parameters are compared to the buoy measurements in Fig. 4. A detailed analysis of the shape of wave spectra is performed in the Supporting Information, see Figures S16-S21. Starting with the directional spread in Fig. 4.a, measurements during wave events are only slightly larger than those modeled without ice attenuation. In contrast, the modeled spread is much larger than observed values when scattering is a dominant term in the attenuation (run S1V1). Reducing the spread to levels comparable to measured values requires a reduction of the scattering coefficient by at least a factor 5, as in the "Anelastic" simulation. This reduced scattering requires stronger dissipation processes to explain the measured wave height attenuation. This attenuation is estimated as the ratio between the "no attenuation" simulation and the measured height, and it varies dramatically in time and across frequencies. Some of these variations are caused by different offshore directions (Fig. 2.b). Still, for similar wave directions, the observed attenuation varies from 80% to 20% between June 20 and June 30 (purple arrows in Fig. 4.c). The gradual variation of wave attenuation in the S1V1 simulation is markedly different from observations which exhibit a sharp cut-off after each wave event such as on July 2 or 8 when no wave energy is measured at buoy 624 (Fig. 4.b-d). The anelastic simulation reproduces that effect which, in the model, is due to displacement of the "break up front" shown with red contours on Fig. 3. When buoy 624 is far from the "break up front", the distance traveled by waves across unbroken ice is large and the attenuation is very strong. In contrast, when the ice is broken up closer to the buoy, the attenuation is much less with an overall wave height attenuation by ice as low as 20%.

The anelastic model scenario presented above is not a unique solution. We assumed an ice thickness $h = 0.77$ m and adjusted the ice flexural strength to $\sigma_c = 0.6$ MPa in order to obtain a spatial extent of broken ice consistent with SAR imagery. Because the ice break-up condition in the model is set by a maximum stress that is proportional to $\sigma_c h^2$, the same results may be obtained by increasing h by a factor a and reducing σ_c by a factor a^2 . Likewise, the magnitude of the anelastic dissipation is controlled by the compliance of the relaxation of dislocations δ , and the number of dislocations per unit area [Cole, 2020]. Since the wave dissipation rate is proportional to $h^3 \delta$, any change in h can be compensated with a change of δ to give the same wave evolution. Conversely, assuming that δ and σ_c are well constrained, it is possible to estimate the ice thickness from SAR imagery using either wave heights and periods at the break-up front or the attenuation of waves in unbroken ice.

For such applications a more realistic dissipation model may be needed. Indeed, the present parameterization tends to overestimate the dissipation of frequencies above 0.085 Hz, as shown in Supporting Figures S16-S20. One possible reason for this model

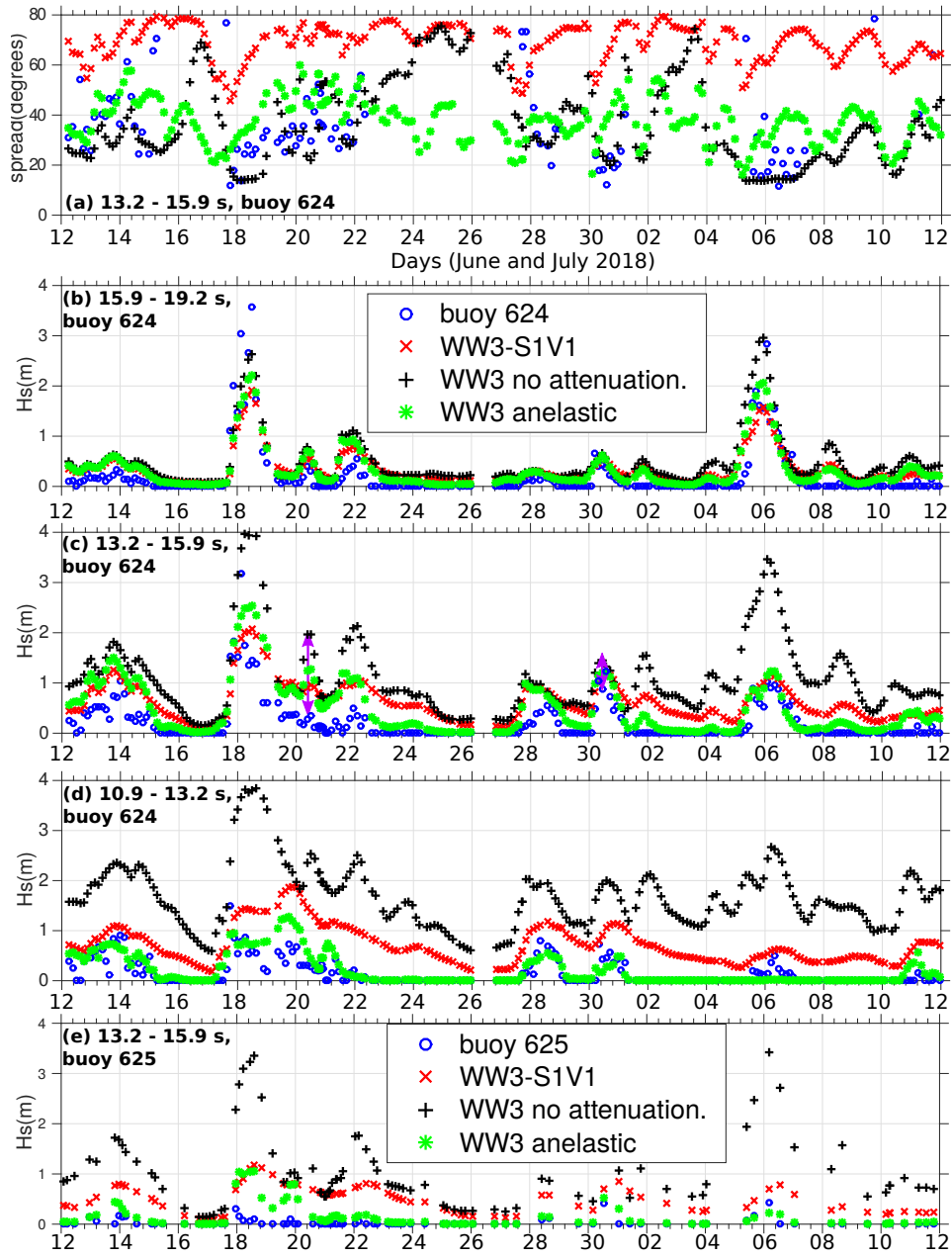


Figure 4. Time series of measured and modeled (a) directional spread and (b-e) wave heights for the ranges of wave periods shown in Fig. 2.a. The model results are shown for the 3 different parameterizations of wave-ice interactions. Purple arrows in (c) point to markedly different attenuation rates, 80% on June 20 and 20% on June 30.

error is the neglected effect of ice in the dispersion relation [Robinson and Palmer, 1990], but other dissipative processes may be involved, including flow in brine pockets during ice deformation, and viscous effects in ice deformation [Meylan *et al.*, 2018; Marchenko and Cole, 2017; Cole, 2020].

4 Conclusions

As storms passed over the open ocean, we measured waves in the ice with narrow directional spreads that are not compatible with existing parameterizations of wave scattering by ice floes. Instead, dissipation associated with ice flexure is a plausible explanation for the previously observed non-linear wave attenuation [Stopa *et al.*, 2018] with weaker attenuation for higher waves. This dissipation provides a transition from a non-broken and highly dissipative flexing ice field to one which is fragmented into small floes with weak attenuation, consistent with our wave and ice observations. This new paradigm also has consequences on how the waves impact the ice. In particular, a dissipation-dominated attenuation concentrates the wave-induced push to the ice around the ice break-up front. In the melting season, the waves may have a more lasting impact as large floes may not reform after each storm, allowing break-up to progress further with the next storm.

Acknowledgments

We thank the New Zealand Navy for buoy deployments, and the EU/ESA Copernicus program for the acquisition of SAR imagery. The analysis was supported by ONR. Buoy data has been uploaded to the UC San Diego Library Digital Collections (<https://doi.org/10.6075/J0V40SM5>), Level-1 SAR wave mode data was provided by the European Space Agency and their processing is supported by Sentinel-1 A Mission Performance Center (Contract No. 4000107360/12/I-LG), and can be viewed at <http://www.ifremer.fr/datavore/exp/dvor/#/s1quicklook>. Finally model simulations are available at <http://tiny.cc/wavesinice>. Comments from anonymous reviewers and discussions with David Cole are gratefully acknowledged.

References

- Ardhuin, F., P. Sutherland, M. Doble, and P. Wadhams (2016), Ocean waves across the Arctic: attenuation due to dissipation dominates over scattering for periods longer than 19 s, *Geophys. Res. Lett.*, *43*, 5775–5783, doi:10.1002/2016GL068204.
- Ardhuin, F., B. Chapron, F. Collard, M. Smith, J. Stopa, J. Thomson, M. Doble, P. Wadhams, B. Blomquist, O. Persson, and C. O. Collins, III (2017), Measuring ocean waves in sea ice using SAR imagery: A quasi-deterministic approach evaluated with Sentinel-1 and in situ data, *Remote sensing of Environment*, *189*, 211–222, doi:10.1016/j.rse.2016.11.024.
- Boutin, G., F. Ardhuin, D. Dumont, C. Sévigny, and F. Girard-Ardhuin (2018), Floe size effects on wave-ice interactions: theoretical background, implementation and applications, *J. Geophys. Res.*, *123*, 4779–4805, doi:10.1029/2017JC013622.
- Cole, D. M. (2020), On the physical basis for the creep of ice: the high temperature regime, *Journal of Glaciology*, *66*(257), 401–414, doi:10.1017/jog.2020.15.
- Cole, D. M., R. A. Johnson, and G. D. Durell (1998), Cyclic loading and creep response of aligned first-year sea ice, *J. Geophys. Res.*, *103*(C10), 21,751–21,758.
- Collins, C., W. E. Rogers, A. Marchenko, and A. V. Babanin (2015), In situ measurements of an energetic wave event in the Arctic marginal ice zone, *Geophys. Res. Lett.*, *42*, 1863–1870, doi:10.1002/2015GL063063.
- Collins, C., M. Doble, B. Lund, and M. Smith (2018), Observations of surface wave dispersion in the marginal ice zone, *J. Geophys. Res.*, *123*, doi:10.1002/2017JC013693.

- Doble, M. J., and J.-R. Bidlot (2013), Wave buoy measurements at the Antarctic sea ice edge compared with an enhanced ECMWF WAM: Progress towards global waves-in-ice modelling, *Ocean Modelling*, *70*, 166–173, doi:10.1016/j.ocemod.2013.05.012.
- Drazen, D., C. Merrill, S. Gregory, A. Fullerton, E. Terrill, and T. de Paolo (2016), Interpretation of in-situ ocean environmental measurements, in *Proc. 31st Symp. on Naval Hydrodynamics, Monterey, CA, Office of Naval Research and Stanford University*, ONR.
- Gloersen, P., and D. J. Cavalieri (1986), Reduction of weather effects in the calculation of sea ice concentration from microwave radiances, *J. Geophys. Res.*, *91*(C3), 3913–3919.
- Herman, A., S. Cheng, and H. H. Shen (2019), Wave energy attenuation in fields of colliding ice floes part 2: A laboratory case study, *The Cryosphere*, *13*, 2911–2914, doi:10.5194/tc-13-2901-2019.
- Kohout, A. L., M. J. M. Williams, S. M. Dean, and M. H. Meylan (2014), Storm-induced sea-ice breakup and the implications for ice extent, *Nature*, *509*, 604–607, doi:10.1038/nature13262.
- Kohout, A. L., M. J. M. Williams, T. Toyota, J. Lieser, and J. Hutchings (2016), In situ observations of wave-induced sea ice breakup, *Deep Sea Res. II*, *131*, 22–27, doi:10.1016/j.dsr2.2015.06.010.
- Liu, A. K., and E. Mollo-Christensen (1988), Wave propagation in a solid ice pack, *J. Phys. Oceanogr.*, *18*, 1702–1712.
- Marchenko, A., and D. Cole (2017), Three physical mechanisms of wave energy dissipation in solid ice, in *Proceedings of the 24th International Conference on Port and Ocean Engineering under Arctic Conditions, June 11-16, 2017, Busan, Korea*, pp. 1378–1381, National Research Council of Canada, ISBN: 978-1-5108-5368-3.
- Meylan, M. H., L. G. Bennetts, and A. L. Kohout (2014), In situ measurements and analysis of ocean waves in the antarctic marginal ice zone, *Geophys. Res. Lett.*, *41*, 5046–5051.
- Meylan, M. H., L. G. Bennetts, J. E. M. Mosig, W. E. Rogers, M. J. Doble, and M. A. Peter (2018), Dispersion relations, power laws, and energy loss for waves in the marginal ice zone, *J. Phys. Oceanogr.*, *123*, 3322–3335, doi:10.1002/2018JC013776.
- Robinson, N. J., Palmer, S. C. (1990). A modal analysis of a rectangular plate floating on an incompressible liquid., *J. of Sound and Vibration*, *142*(3), 452–460, doi:10.1016/0022-460X(90)90661-I.
- Spreen, G., L. Kaleschke, and G. Heygster (2008), Sea ice remote sensing using AMSR-E 89-GHz, *J. Geophys. Res.*, *113*(5), C02S03, doi:10.1029/2005JC003384.
- Squire, V. A. (2020), Ocean wave interactions with sea ice: A reappraisal, *Annu. Rev. Fluid Mech.*, *52*, 37–60, doi:10.1146/annurev-fluid-010719-060301.
- Stopa, J. E., F. Ardhuin, and F. Girard-Ardhuin (2016), Wave climate in the Arctic 1992-2014: seasonality and trends, *The Cryosphere*, *10*, 1605–1629, doi:10.5194/tc-10-1605-2016.
- Stopa, J. E., P. Sutherland, and F. Ardhuin (2018), Strong and highly variable push of ocean waves on southern ocean sea ice, *Proc. Nat. Acad. Sci.*, *115*(23), 5861–5865, doi:10.1073/pnas.1802011115.
- Sutherland, P., and D. Dumont (2018), Marginal ice zone thickness and extent due to wave radiation stress, *J. Phys. Oceanogr.*, *48*, 1885–1901, doi:10.1175/JPO-D-17-0167.1.
- The WAVEWATCH III[®] Development Group (2019), User manual and system documentation of WAVEWATCH III[®] version 6.07, *Tech. Note 333*, NOAA/NWS/NCEP/MMAB, College Park, MD, USA, 465 pp. + Appendices.
- Thomson, J., S. Ackley, F. Girard-Ardhuin, F. Ardhuin, A. Babanin, G. Boutin, J. Brozena, S. Cheng, C. Collins, M. Doble, C. Fairall, P. Guest, C. Gebhardt, J. Gemmrich, H. C. Graber, B. Holt, S. Lehner, B. Lund, M. H. Meylan, T. Maksym, F. Montiel, W. Perrie, O. Persson, L. Rainville, W. E. Rogers, H. Shen, H. Shen,

- 310 V. Squire, S. Stammerjohn, J. Stopa, M. M. Smith, P. Sutherland, and P. Wadhams
 311 (2018), Overview of the arctic sea state and boundary layer physics program, *J.*
 312 *Geophys. Res.*, *123*, doi:10.1002/2018JC013766.
- 313 Toffoli, A., L. G. Bennetts, M. H. Meylan, C. Cavaliere, A. Alberello, J. Elsnab, , and
 314 J. P. Monty (2015), Sea ice floes dissipate the energy of steep ocean waves, *Geophys.*
 315 *Res. Lett.*, *42*, 8547–8554, doi:10.1002/2015GL065937.
- 316 Wadhams, P. (1988), Winter observations of iceberg frequencies and sizes in the south
 317 atlantic ocean, *J. Geophys. Res.*, *93*, 3583–3590.
- 318 Williams, T. D., L. G. Bennetts, V. A. Squire, D. Dumont, and L. Bertino (2013),
 319 Wave-ice interactions in the marginal ice zone. part 1: Theoretical foundations,
 320 *Ocean Modelling*, *70*, 81–91, doi:10.1016/j.ocemod.2013.05.010.

Supporting Information for "Ice break-up controls dissipation of wind-waves across Southern Ocean sea ice"

Fabrice Ardhuin¹, Mark Otero¹, Sophia Merrifield¹, Antoine Grouazel², and Eric Terrill¹

¹Scripps Institution of Oceanography, La Jolla, California

²Univ. Brest, CNRS, IRD, Ifremer, Laboratoire d'Océanographie Physique et Spatiale (LOPS), IUEM, Brest, France

Contents of the Supplementary information

1. Introduction
2. Movie S1
3. Figures S1 to S21. Note that S16 to S21 are included in the following discussion.
4. Discussion of wave spectral shapes and possible linear dissipations proportional to the frequency to a power n .

1. Introduction

This Supporting information contains a movie that complements Figure 1 and helps visualize buoy locations relative to the ice edge in the context of the storms observed. The supplementary figures S1-S15 provide a more detailed view of the ice and wave features observed on July 5 and 6, complementing figure 4. Figures S16 to S21 are associated with the discussion of spectral shapes and the possible identification of a linear dissipation process proportional to f^n , following the type of analysis performed by Meylan et al. (2018).

2. Movie S1

Location of buoys 623, 624, and 625 in the context of the evolving sea ice concentration field estimated from the Advanced Microwave Scanning Radiometer 2 and processed by the University of Bremen (Spreen et al. 2008). Maximum floe size contour $D_{\max} = 300$ m, wave heights, and mean directions are taken from the the "Anelastic" model run.

3. Figures S1-S15

Quicklooks of SAR images labeled 1-15 in Fig. 3.

These can be obtained from <http://www.ifremer.fr/datavore/exp/dvor/#/s1quicklook>

Images are displayed in acquisition geometry with range (satellite cross-track direction) on the x -axis and azimuth (satellite along-track direction) on the y -axis. The original Level 1 product, with a resolution of 4 m, is subsampled to a 600 x 600 pixel image of 35 m resolution. The grey scale representing radar backscatter after SAR processing is automatically adjusted in each image to linearly cover the 1st to 99th percentiles of the image intensity in order to maximize contrast. The mean sea surface roughness value (μ) is indicated on each figure. The samples shown in Fig. 3 were rotated to orient North upward.

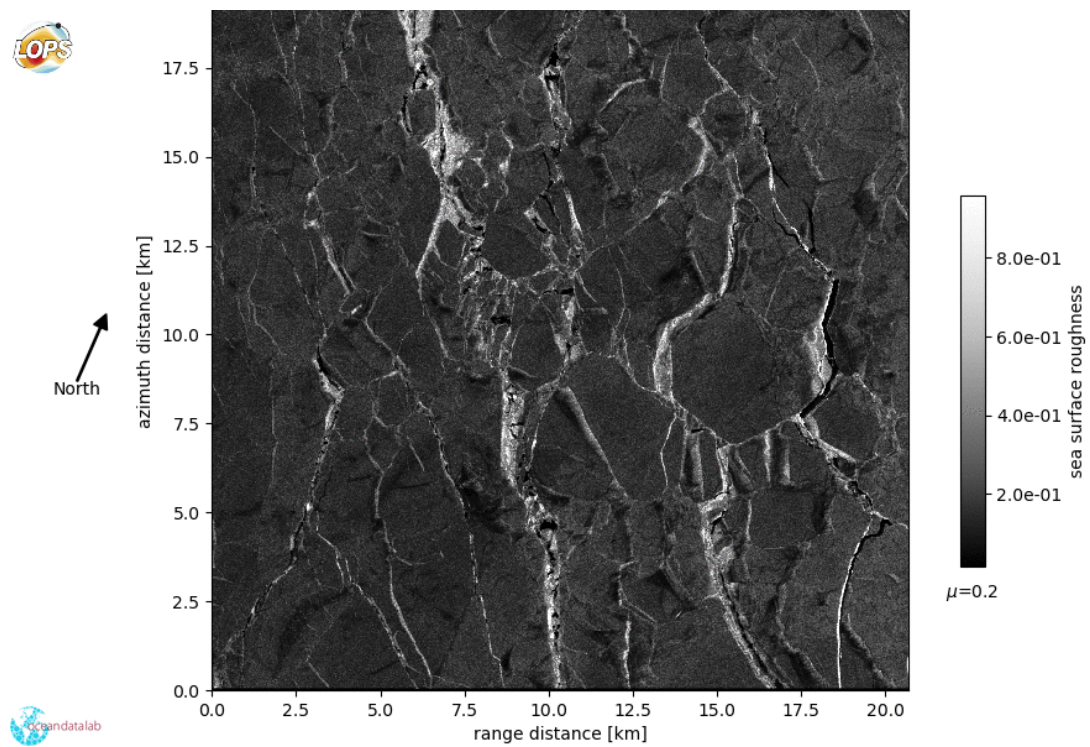


Figure S1. SAR image acquired 2018/07/05 at 06:01:08

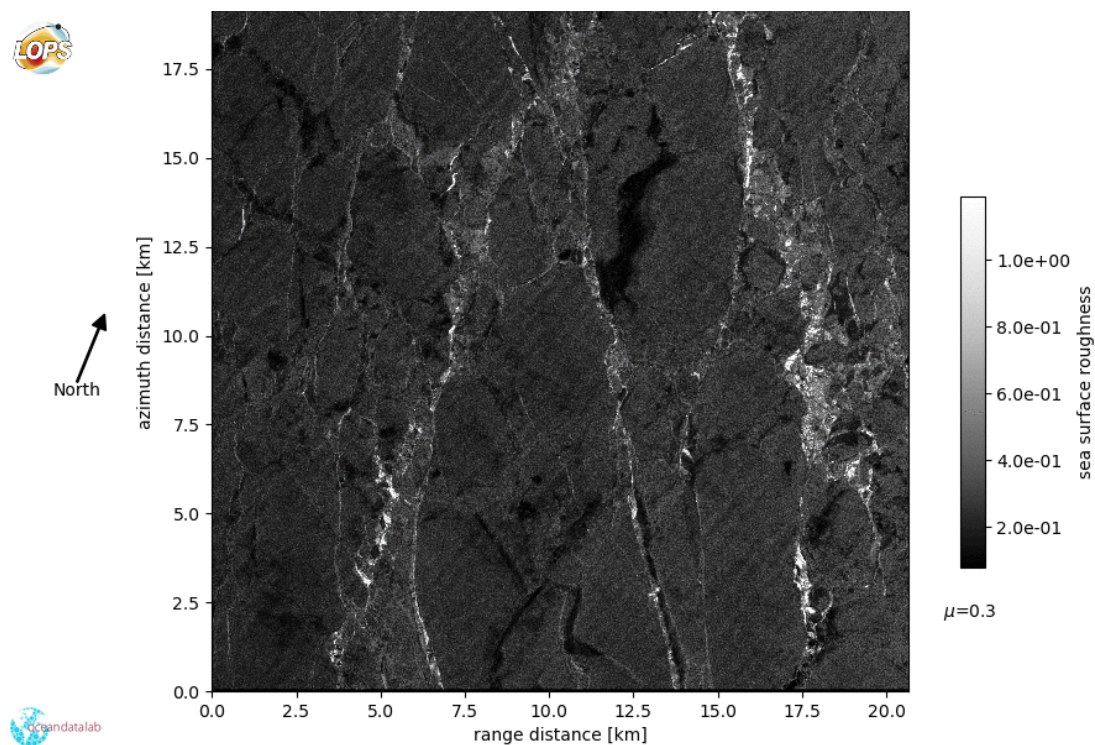


Figure S2. SAR image acquired by Sentinel 1B on 2018/07/05 at 06:01:38

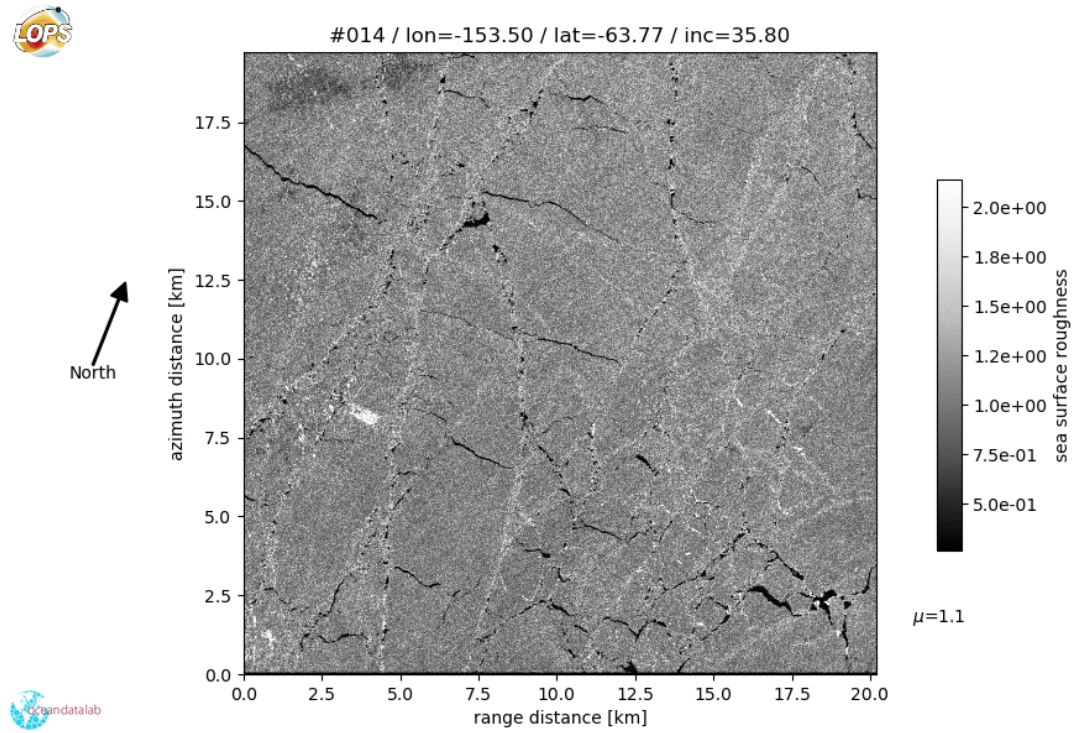


Figure S3. SAR image acquired by Sentinel 1B on 2018/07/05 at 06:01:52

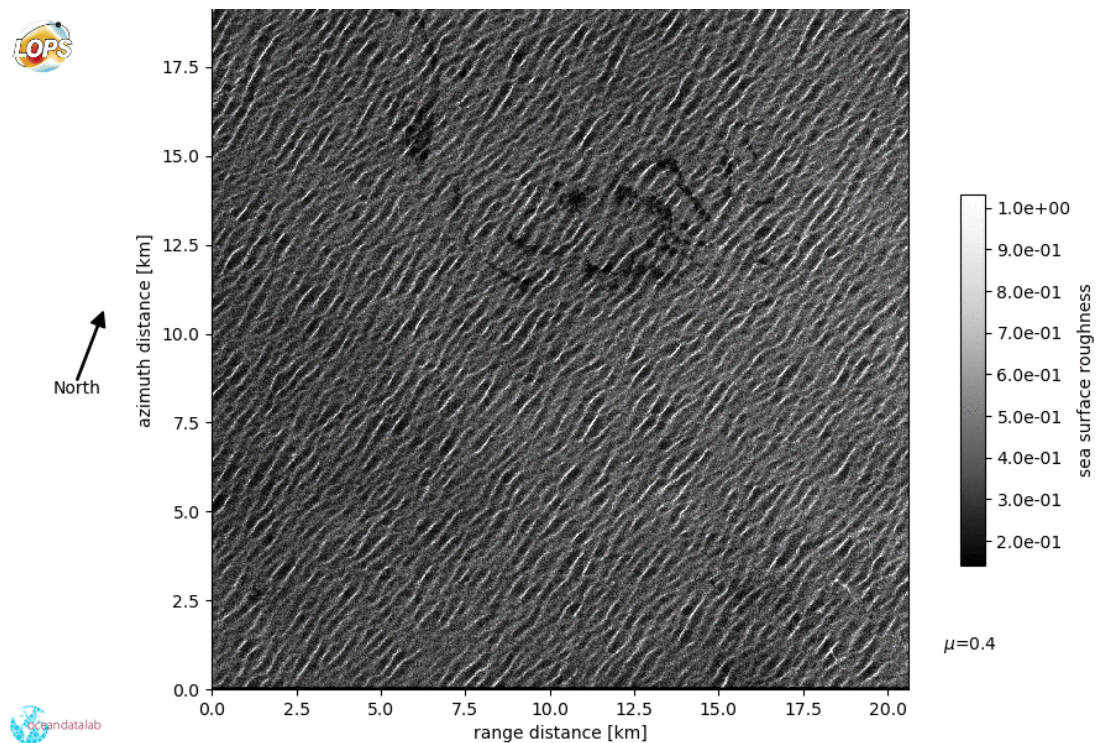


Figure S4. SAR image acquired by Sentinel 1B on 2018/07/05 at 06:02:07

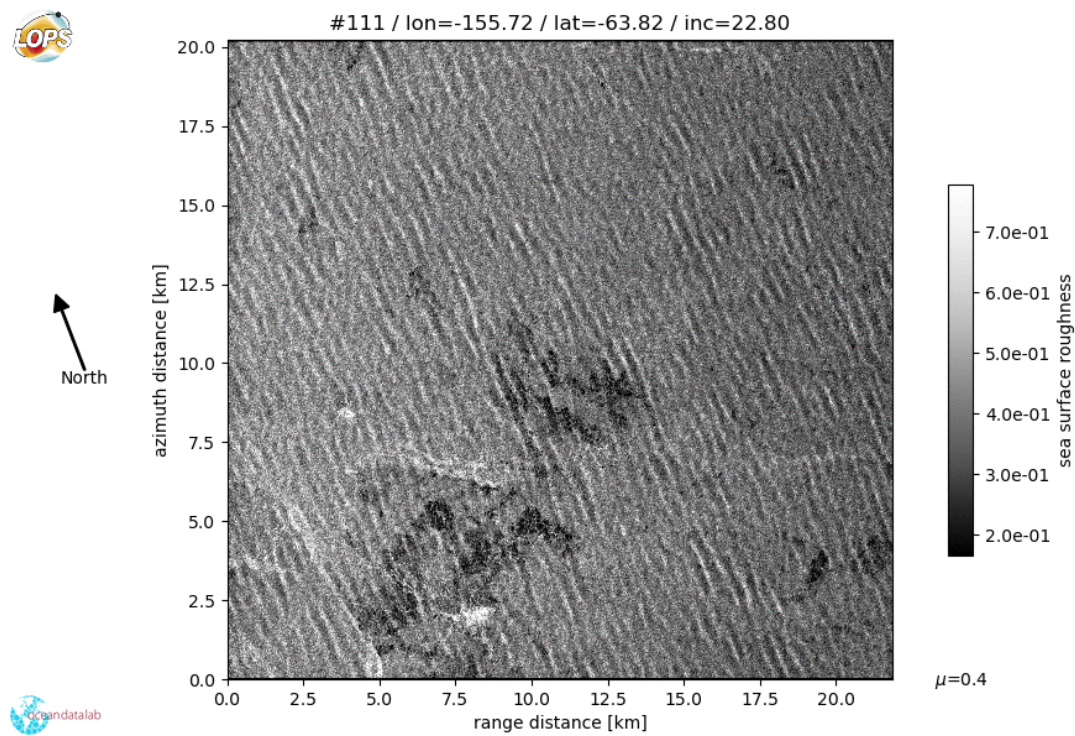


Figure S5. SAR image acquired by Sentinel 1A on 2018/07/05 at 14:52:37

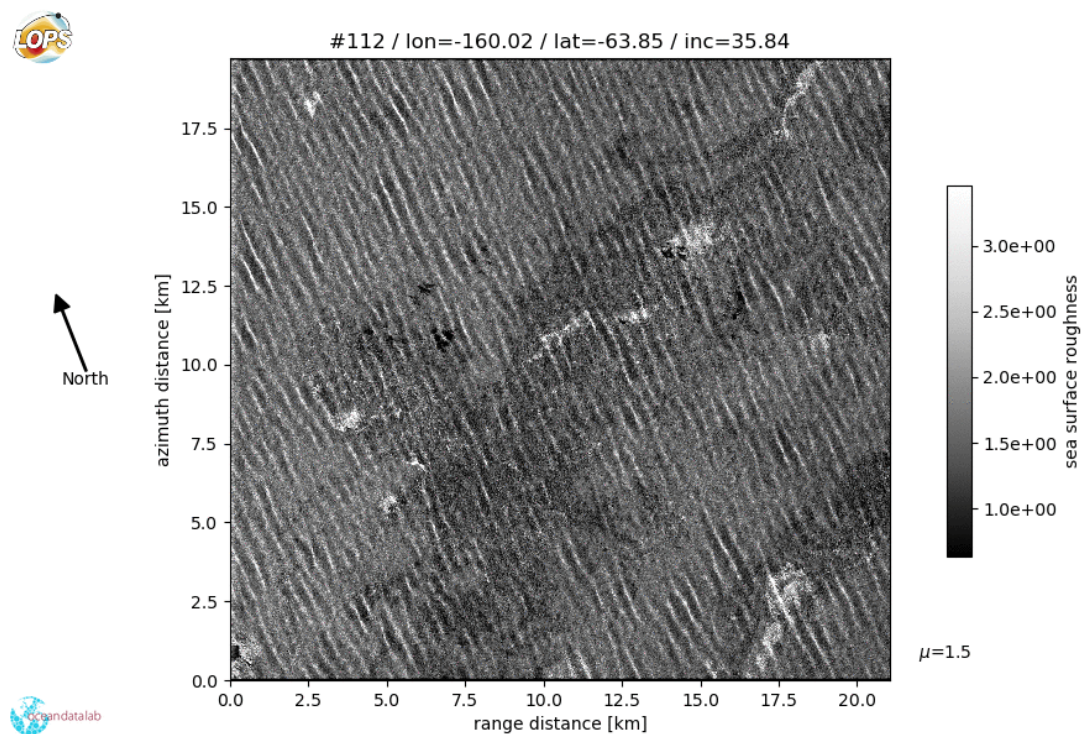


Figure S6. SAR image acquired by Sentinel 1A on 2018/07/05 at 14:52:52

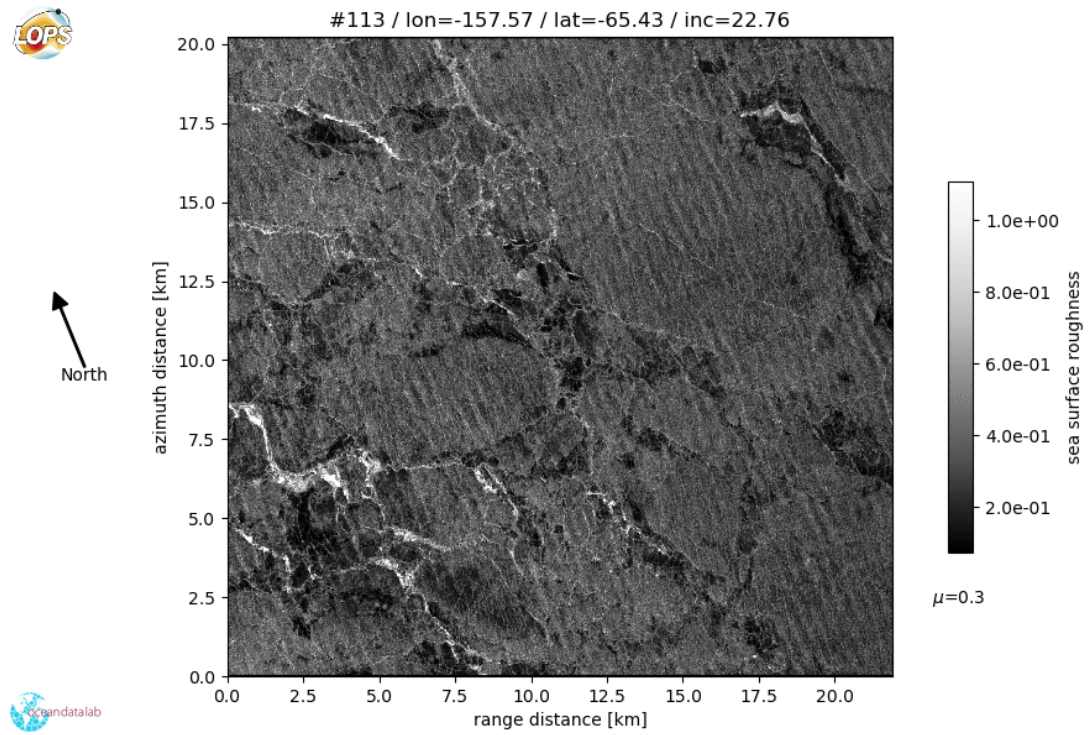


Figure S7. SAR image acquired by Sentinel 1A on 2018/07/05 at 14:53:06

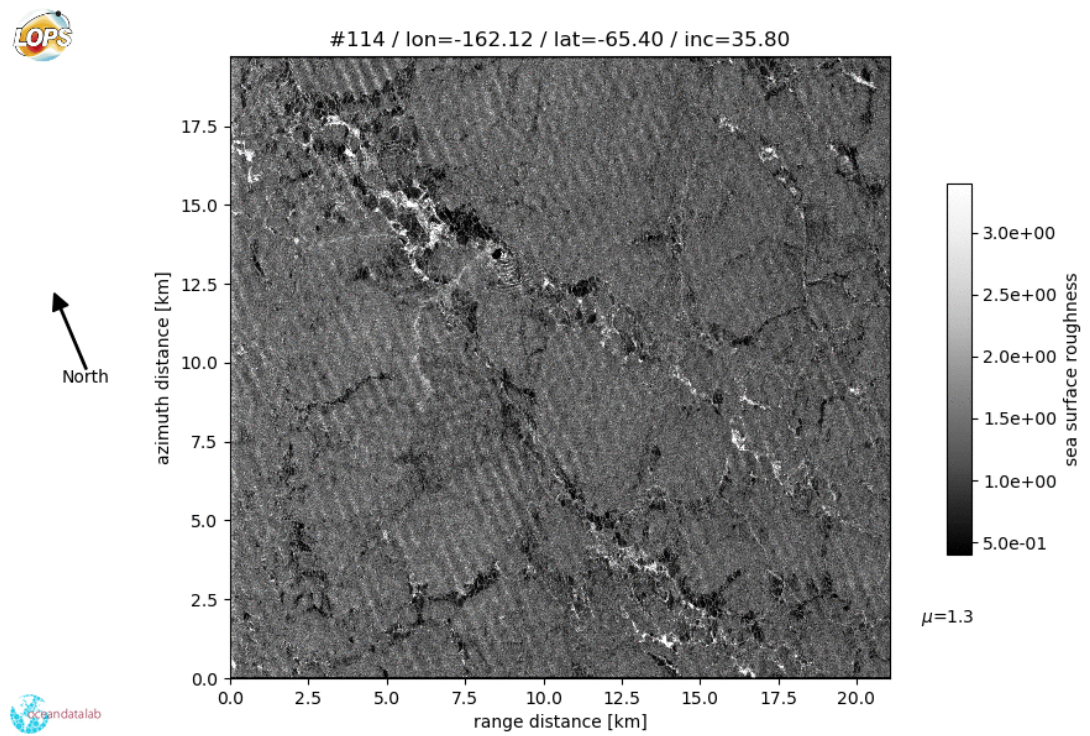


Figure S8. SAR image acquired by Sentinel 1A on 2018/07/05 at 14:53:21

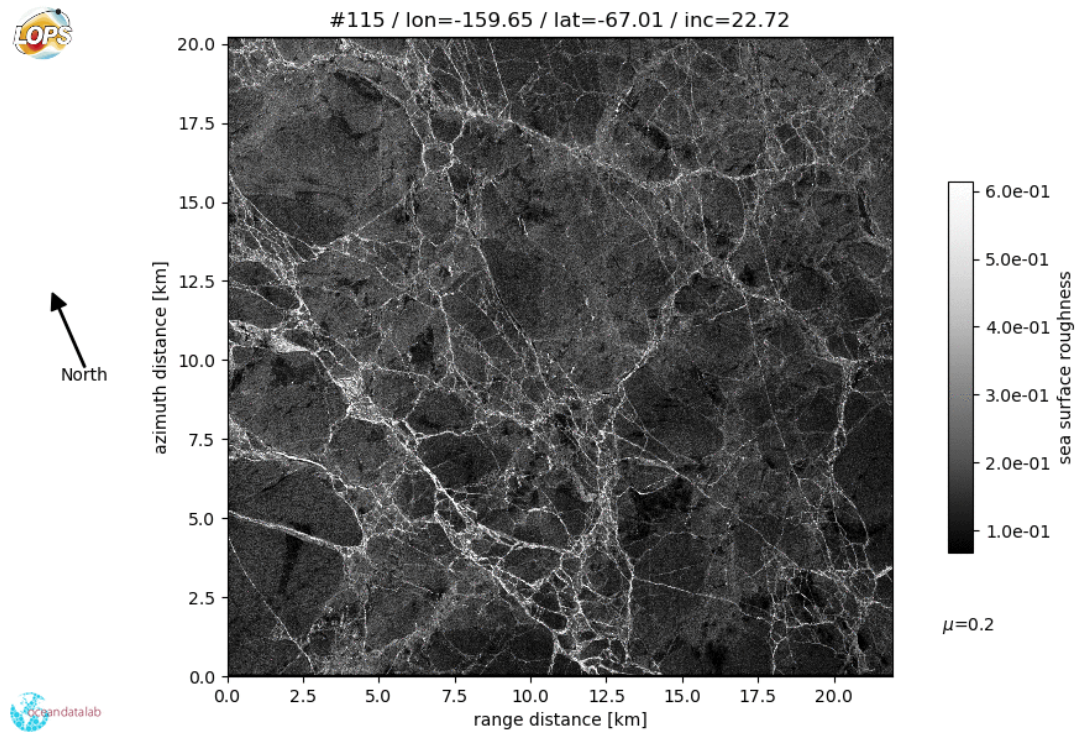


Figure S9. SAR image acquired by Sentinel 1A on 2018/07/05 at 14:53:3

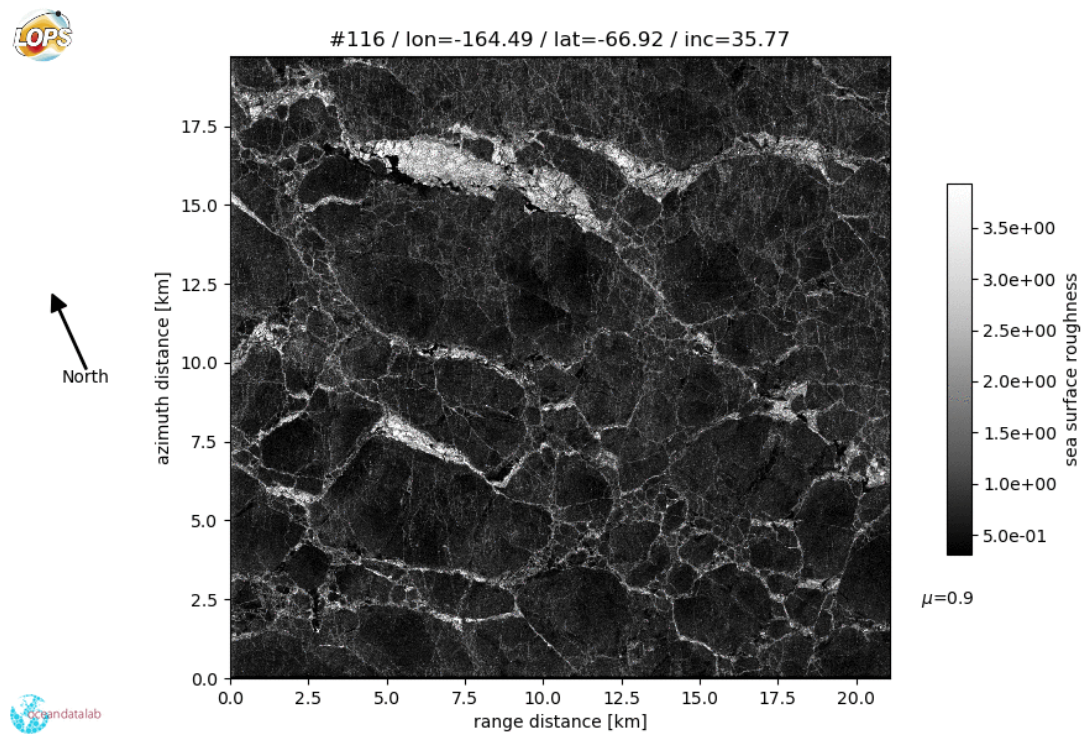


Figure S10. SAR image acquired by Sentinel 1A on 2018/07/05 at 14:53:50

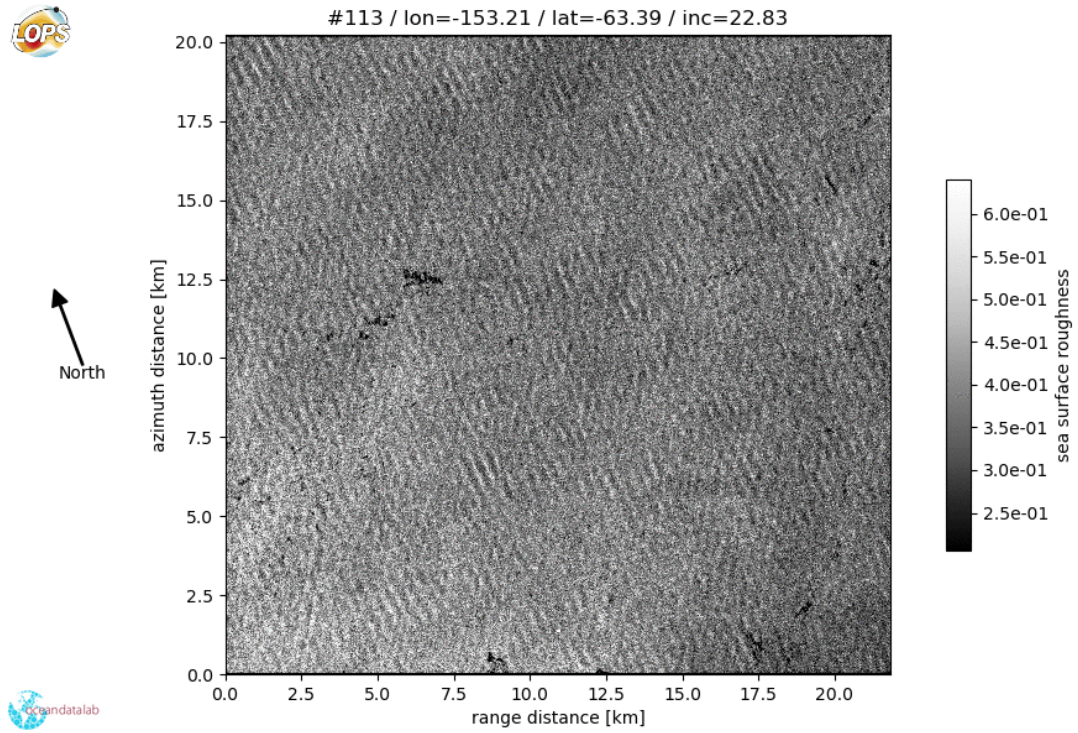


Figure S11. SAR image acquired by Sentinel 1B on 2018/07/06 at 14:43:34

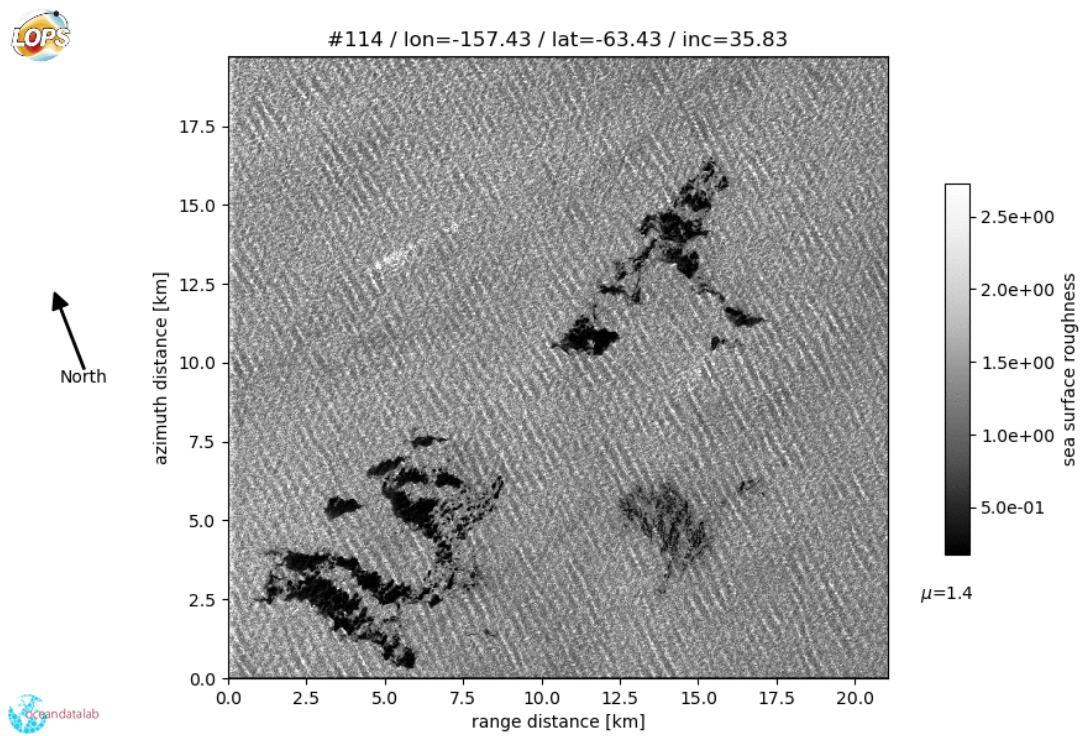


Figure S12. SAR image acquired by Sentinel 1B 2018/07/06 at 14:43:49.

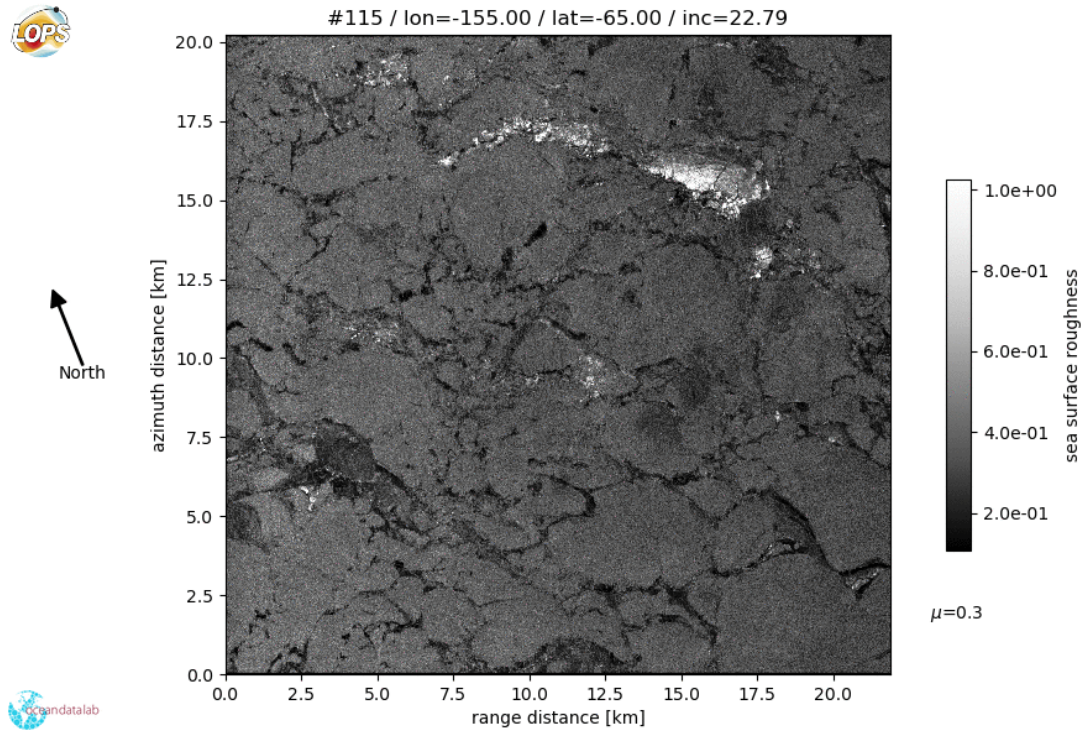


Figure S13. SAR image acquired by Sentinel 1B on 2018/07/06 at 14:43:03.

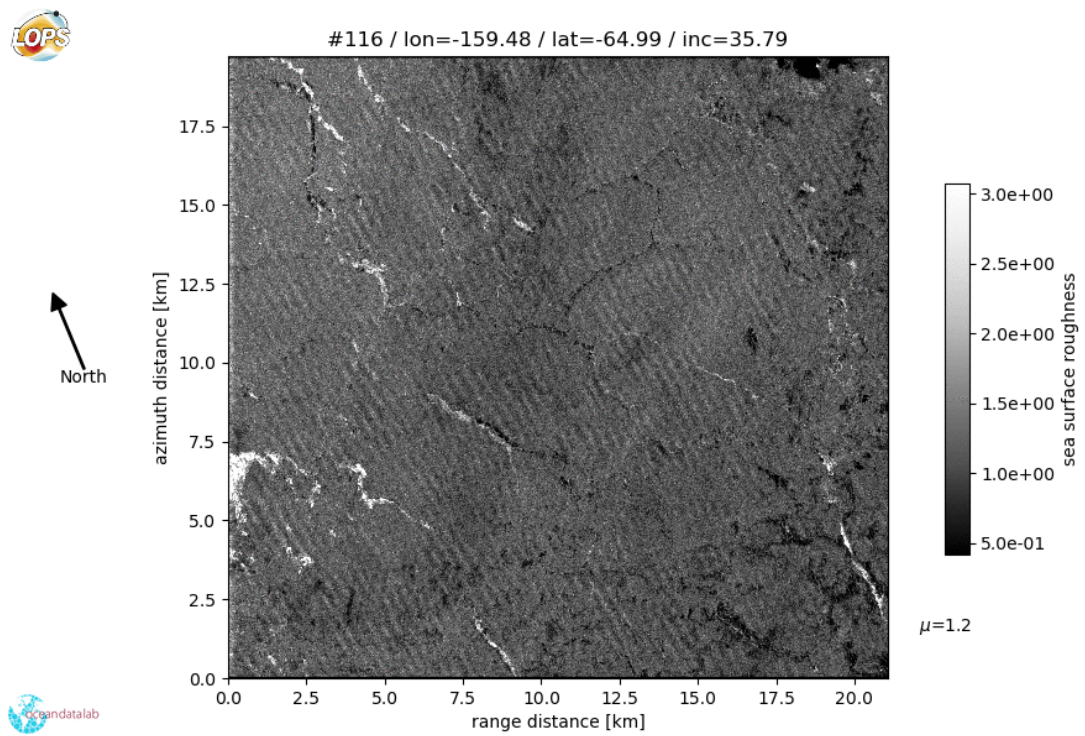


Figure S14. SAR image acquired by Sentinel 1B on 2018/07/06 at 14:44:18.

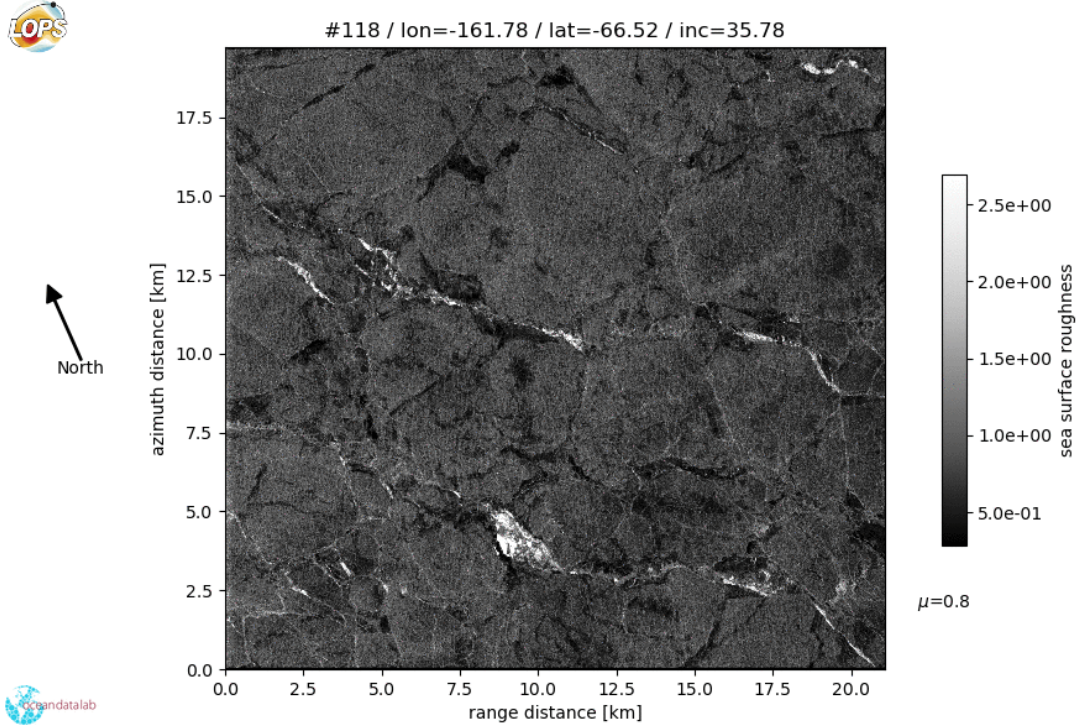


Figure S15. SAR image acquired by Sentinel 1B on 2018/07/06 at 14:44:50.

4. Discussion and Figures S16-S21

Whereas the main body of the paper focuses on the temporal evolution of wave properties, here we examine the spectral distribution of wave energy which provides a complementary perspective of possible dissipation processes. Indeed, Meylan et al. (2018) have argued that different dissipation processes have distinct spectral signatures. This idea has been used to characterize the effect of frazil and pancake ice on spectral shape.

This approach is particularly well suited for linear processes. Considering a 1-dimensional propagation along the x axis, the wave spectrum $E(x, t, f)$ is attenuated by a source function $S_{ice}(x, t, f) = a(x)f^m E(x, t, f)$, namely

$$\partial E(x, t, f) / \partial t + \partial [C_g(f) E(x, t, f)] / \partial x = S_{ice}(x, t, f). \quad (1)$$

Using the method of characteristics this gives,

$$E(x, t, f) = E(x_0, t - C_g(f) \times (x - x_0), f) \times \exp \left[f^m / C_g(f) \int_{x_0}^x a(x') dx \right], \quad (2)$$

which can be generalized to any polynomial function of the frequency. Also, for a simple dispersion relation, $C_g(f)$ is also a power law of f and then can be combined with S_{ice} to give,

$$E(x, t, f) = E(x_0, t - C_g(f) \times (x - x_0), f) \times \exp \left[f^n \int_{x_0}^x b(x') dx \right]. \quad (3)$$

Without ice effect, the spectrum would have been

$$E_{noice}(x, t, f) = E(x_0, t - C_g(f) \times (x - x_0), f), \quad (4)$$

such that the power n can be obtained by taking the log of the ratio $r(x, t, f) = \log [E(x, t, f) / E_{noice}(x, t, f)]$.

From values of r at two frequencies, f_i and f_j , we get,

$$n(x, t, f_i, f_j) = \log (r(x, t, f_i) / r(x, t, f_j)) / \log (f_i / f_j) \quad (5)$$

For Airy waves, $n = m + 1$ and the wavenumber k is proportional to f^2 . For viscous friction S_{ice} is proportional to $k\sqrt{f}$ and thus $m = 2.5$ and $n = 3.5$. For anelastic dissipation, we expect a much steeper variation with frequency, as illustrated in Figure S16, because the stress and strain are both proportional to the surface curvature, giving a k^4 contribution, that is reduced a little by the $f^{-0.5}$ variation of the phase shift between stress and strain Cole et al. (1998), leading to $n = 9.5$.

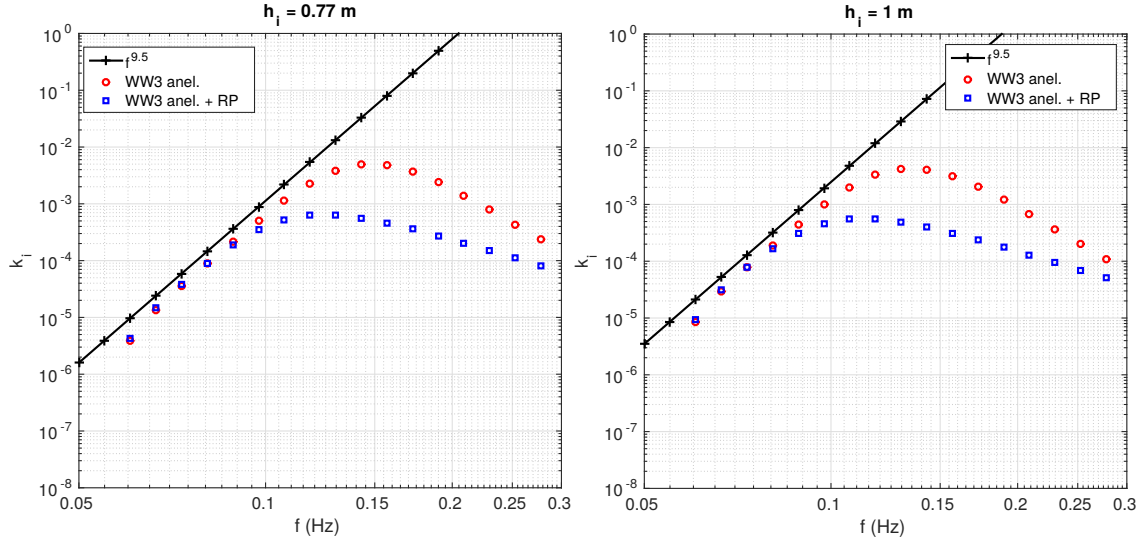


Figure S16. Amplitude decay (imaginary wavenumber) as a function of wave frequency for the anelastic model of Cole et al. (1998) when using a Robinson-Palmer (blue) or Airy (red) dispersion relation.

However, this is only valid as long as the elastic contribution to the wave energy can be neglected, which is a function of the ice thickness. Indeed, the conservation of the energy flux of waves propagating from the open water under the ice leads to a smaller wave amplitude.

In order to be fully consistent (which was not the case in the main body of the paper, for the sake of simplicity), the ice thickness should also be taken into account in the wave dispersion relation. For this we may use the dispersion relation by Robinson and Palmer (1990). This gives a transition of the wavenumber from $k \propto f^2$ at low frequencies to $k \propto f^{0.5}$ at high frequencies, and $C_g \propto f^{-1}$ to $C_g \propto f^{0.5}$. That effect of dispersion depends on the ice thickness, and for the value $h_i = 0.77$ m used in the paper, it is significant for wave frequencies above 0.1 Hz.

With all this in mind, we can now look at frequency spectra from the buoy measurements and model results. The average spectra at the off-ice buoy 623 and in-ice buoy 624 are shown in Figure S17.

From the monthly-averaged spectra, it is clear that below 0.08 Hz the model underestimates the off-ice wave energy. Above 0.08 Hz, the shape of the modeled spectra is too steep for the anelastic dissipation, and with about the right shape but too high by a factor 10 or more for the viscous dissipation. As shown in Figure S18, part of the discrepancy in the anelastic model could be due to the use of the Airy dispersion relation, with the Robinson and Palmer (1990) dispersion working better especially if we use an ice thicknesses larger than the 0.77 m used all the model results shown here.

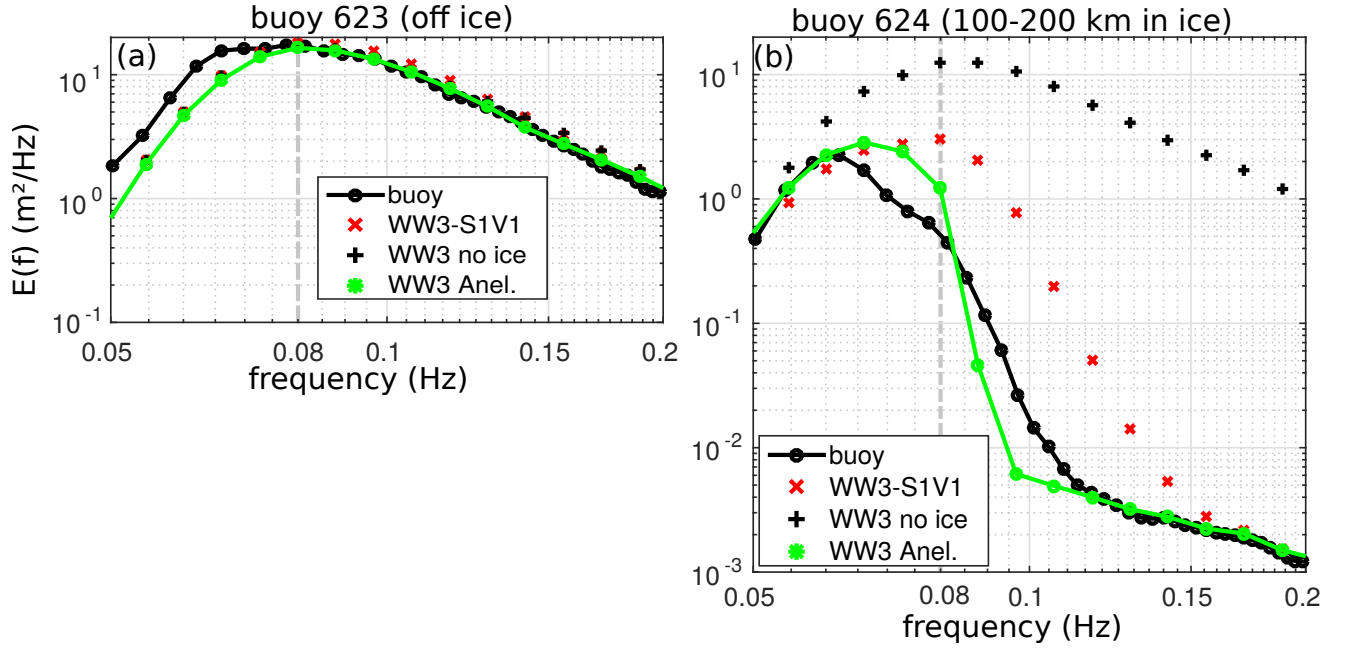


Figure S17. Mean spectra at buoys 623 and 624, from June 12 to July 12. A f^{-2} noise floor was added to the model to make it comparable to the measurements.

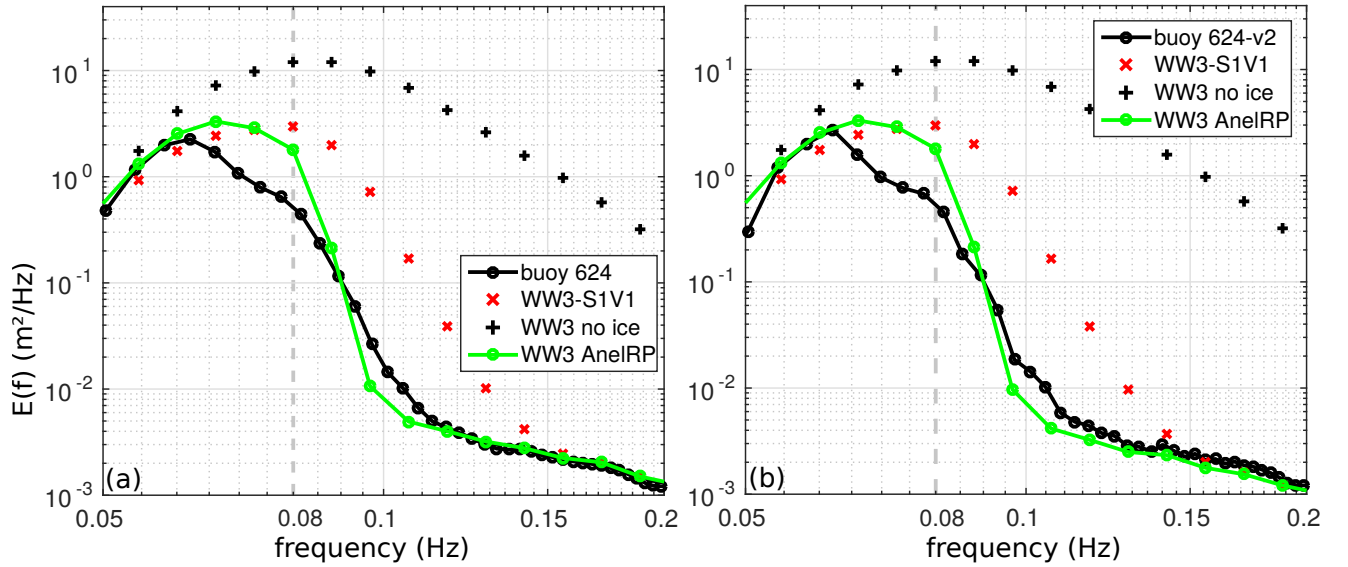


Figure S18. Mean spectra at buoy 624, from June 12 to July 12 with (a) the Anelastic WW3 model run now including the Robinson and Palmer dispersion relation, and (b) without the 3-point smoothing included in the data processing, giving a 30% lower spectral density at $f=0.97$ Hz.

Possibly the frequency smoothing that is used in the buoy data processing also contributes to that difference. Indeed, the default data processing has each spectral component obtained with a 3-point frequency (Hann filter) smoothing with weights $[0.25 \ 0.5 \ 0.25]$. That processing step tends to reduce the spectral slope at both 0.08 Hz (near the typical spectral peak) and at 0.097 Hz (where the spectrum approaches the noise level). Also, we note that when averaged over 1 day, the spectral estimate uses 128 degrees of freedom, hence a $\pm 24\%$ error at the 95% confidence level, which may be used to estimate an error on the fitted power law.

We may now take a look at the values of n estimated from the data. In practice we have computed used the discrete frequencies $f_{13} = 0.0815$, $f_{14} = 0.0854$, $f_{15} = 0.0894$, $f_{16} = 0.0933$, $f_{17} = 0.0972$ to compute $n_{14,15}$, $n_{15,16}$, $n_{16,17}$ and $n_{14,17}$, using daily-averaged spectra. The same n parameters were computed from the modeled spectra after their interpolation

on the observed frequency grid. The first result is that, even in the model runs, there is a wide variability of n . Also, on most of the days the energy level is below the noise floor and n cannot be estimated, so that any estimate of n will be biased towards the strong energy event.

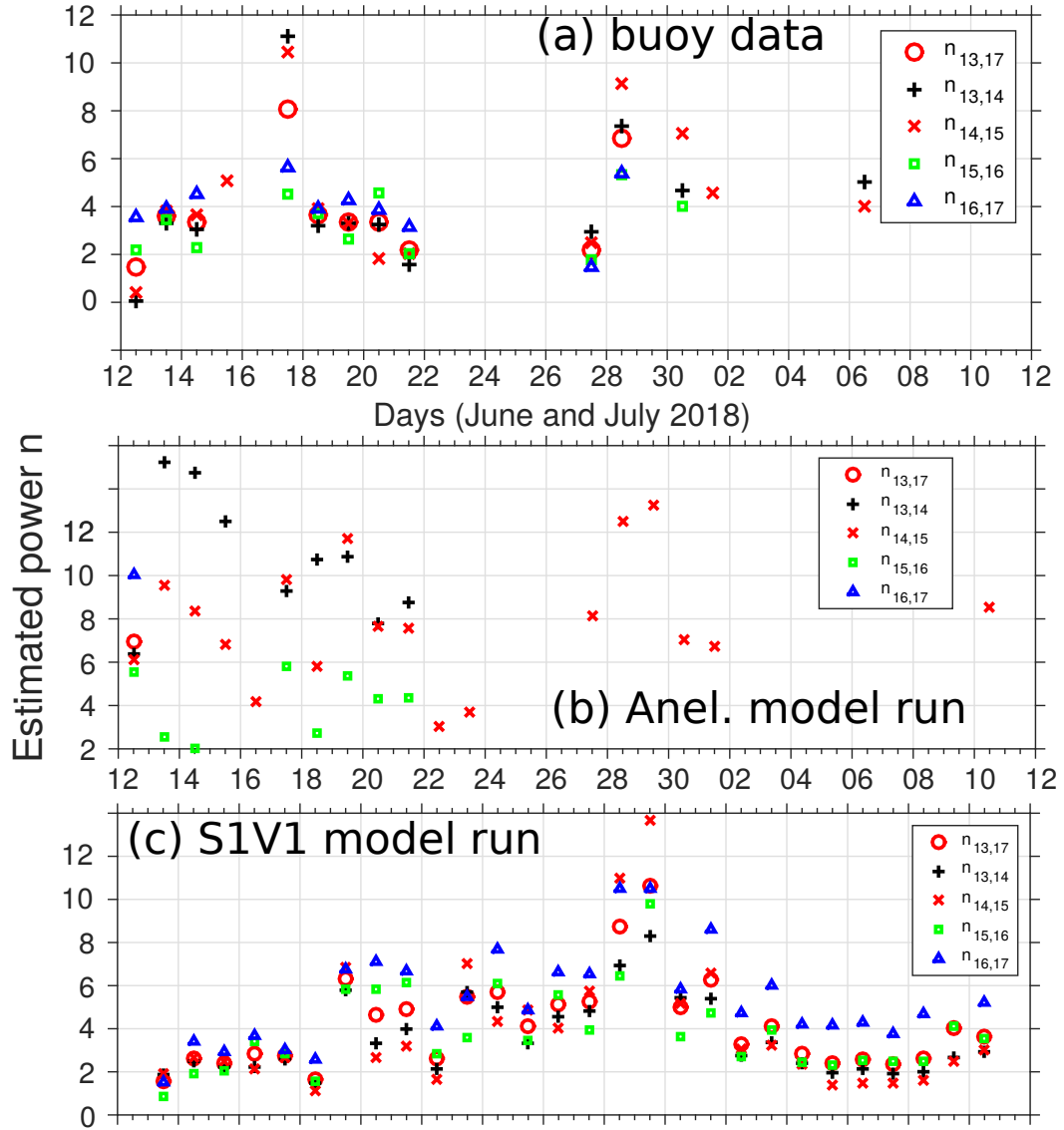


Figure S19. Dissipation power law parameters $n_{14,15}$, $n_{15,16}$, $n_{16,17}$ and $n_{14,17}$ estimated from daily-averaged (a) measured spectra, (b) modeled spectra with anelastic dissipation (c) modeled spectra with viscous dissipation. Estimates are only available when the spectrum is larger than 2 times the mean noise level.

Daily average estimates of n range from 0.2 to 11. The scatter is even larger for the anelastic model run, and the scattering-viscous model run (S1V1) has a large range of n values, showing that the simple linear attenuation of unidirectional waves does not represent well the more complex situation with waves from all directions. In order to understand a bit better this variability we now look at spectra for individual days, overlaying analytical examples of attenuations with powers $n = 9.5$, $n = 4$ and $n = 3$.

It is particularly interesting to contrast the spectral shape on June 17 at the start of a wave event, with a very steep high frequency decay consistent with $5 < n < 11$, and the next day with $n \approx 4$ (Figure S20). In the chosen frequency range (above 0.08 Hz) the model performs well off the ice at buoys 623.

On the wave event from 27 to 28 June, n estimated from the buoy data changes from 2 to 6 before the energy level disappears below the noise level on the 29th whereas a constant attenuation rate would have given a strong signal. Steep spectra can also be found such as on July 1st (bottom line, figure S21), but n cannot be estimated because only $E(f_{14})$ is well above the noise.

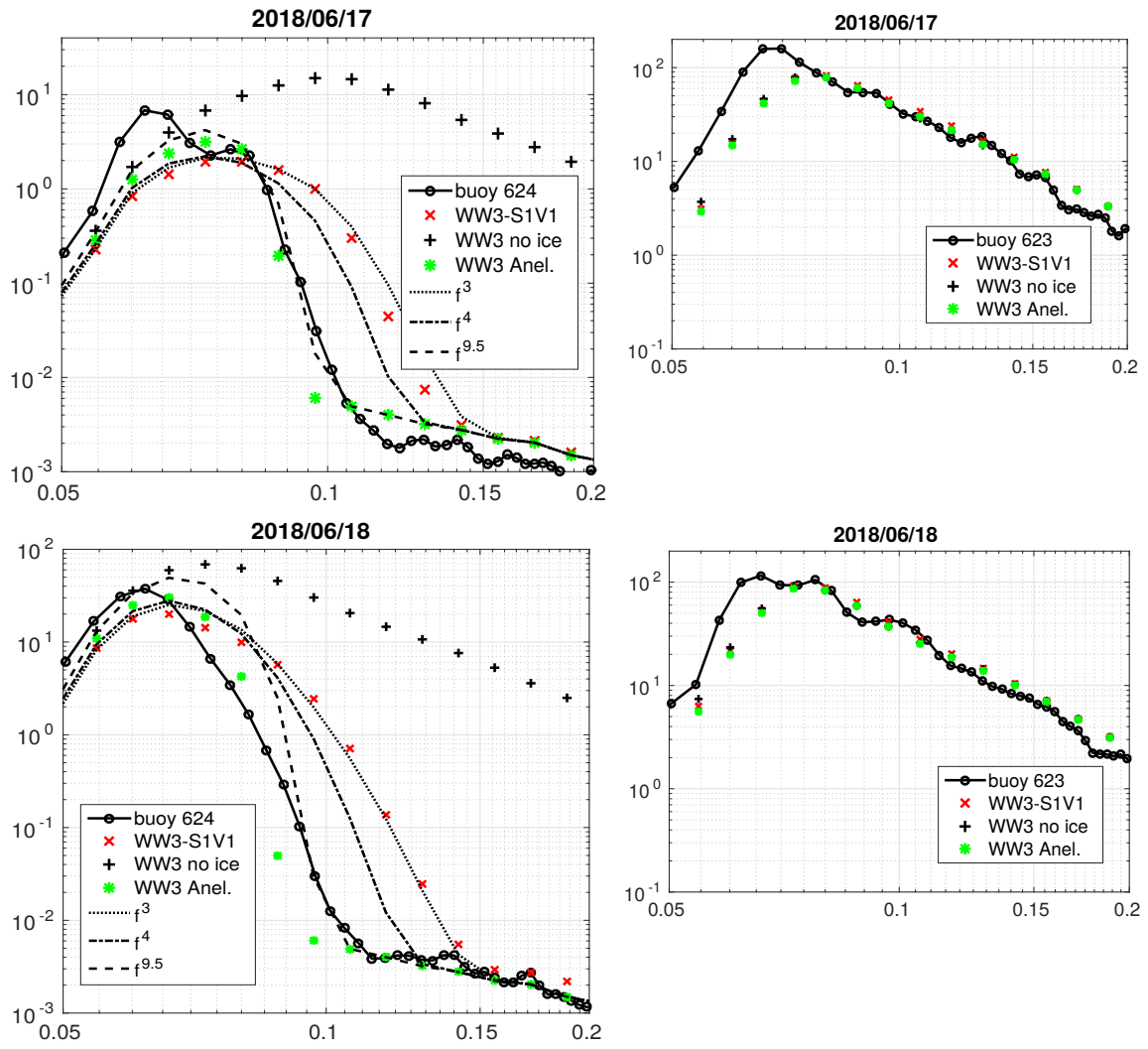


Figure S20. Measured and modelled spectra on June 17 (top) and June 18 (bottom), at buoys 624 (left) and 623 (right).

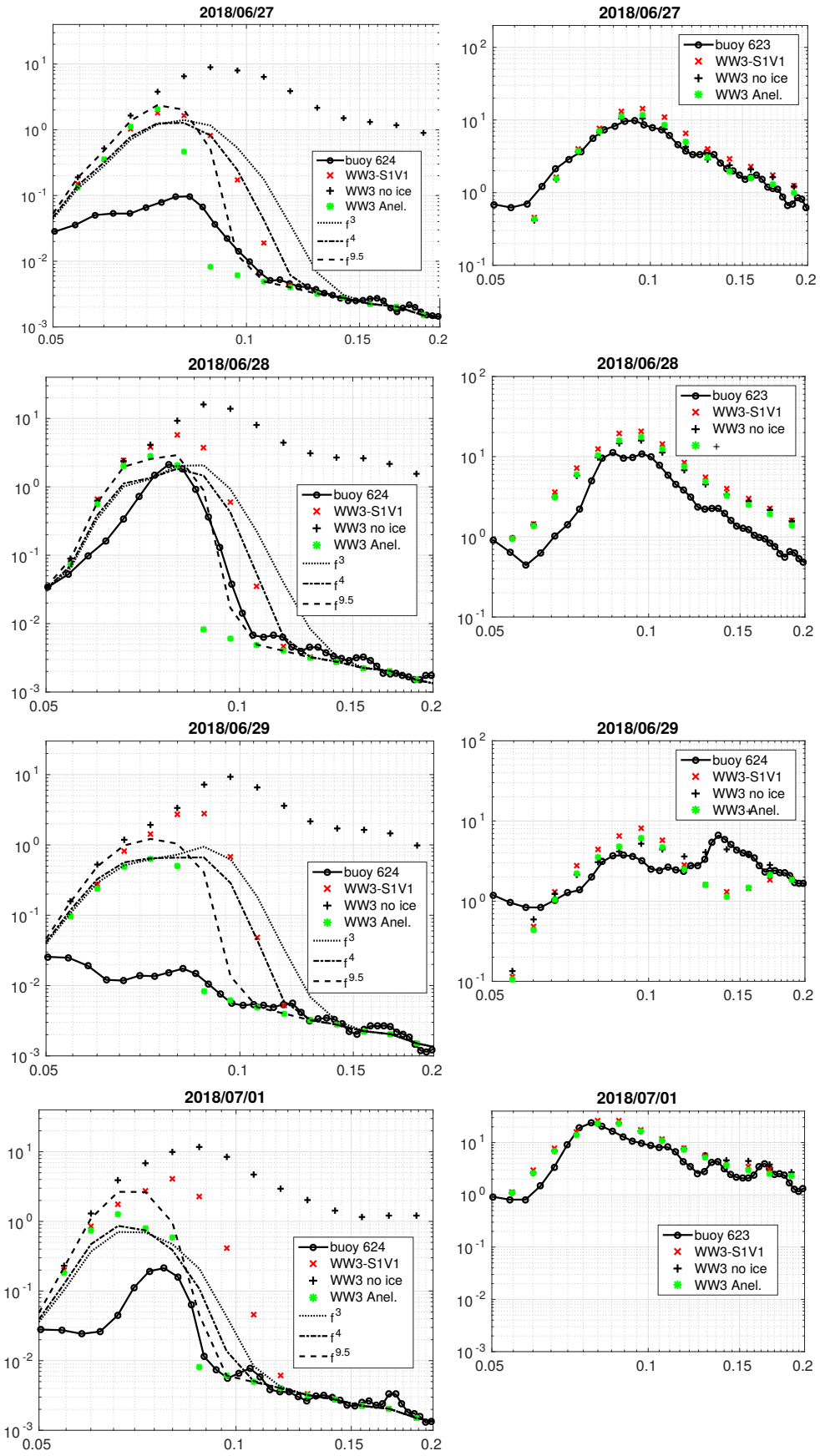


Figure S21. Measured and modelled spectra on (from top to bottom), June 27, June 28, June 29, and July 1st, at buoys 624 (left) and 623 (right).